Supplementary Information to "In-situ Electronic Probing of Photoconductive Trap States for the Catalytic Reduction of CO_2 by $In_2O_{3-x}OH_y$ Nanorods".

Joel Y.Y Loh [a], Nazir P. Kherani[a,b]

[a] *Electrical and Computing Engineering, University of Toronto, Toronto, Ontario M5S 3G4, Canada.*

[b] *Material Science and Engineering, University of Toronto, Toronto, Ontario M5S 3E4, Canada.*

Corresponding author: kherani@ecf.utoronto.ca

Contextual Information

The information presented in Figure 1a was reproduced from the reference "Spatial Separation of Charge Carriers in $In_2O_{3-x}(OH)_y$ Nanocrystal Superstructures for Enhanced Gas-Phase Photocatalytic Activity," *ACS Nano*, 2016, vol. 10, no. 5." wherein samples from the same batch were studied in the current manuscript. The CO production rate was measured in a batch photo-thermal reactor by introducing 14 psi of H_2 and an additional 14 psi of C13 isotope CO_2 to a sample deposited on quartz fiber substrates which were pre-heated to 150°C. After 12 hours under a xenon arc lamp and 150°C reactor temperature, an SRI 8610 gas chromatograph was used to determine the CO yield of the output gas, while a GC mass spectrometer was used to verify that C13 CO was produced. XPS measurements were taken with an ESCALAB XPS microprobe instrument, wherein the O1s scans all show a lattice oxygen peak and an hydroxide associated shoulder to the lattice oxygen peak. By deconvoluting the total area into lattice oxygen, oxygen vacancies and hydroxide group peaks the areas of the peaks associated with oxygen vacancies and hydroxide group were normalized as the OH + O_{vac} ratio determined by dividing the area of OH sub-peak and the $O_{vacancy}$ sub-peak over the lattice oxide sub-peak: 1-((O_{vac}+OH)/(O)). The calculations showed that the O_{vac}+OH ratio had a small decrease with increasing aging time, whereas CO rates increase with aging time.

Experimental Information

$In_2O_{3-x}OH_y$ nanorod structures discussed in this paper were fabricated through the following steps: 0.397g of $InCl_3$ was dissolved in 6ml ethanol with stirring, a separate mixture of 2.5ml urea and 7.5ml ethanol and 2ml H_2O was mixed in the $InCl_3$, creating a white suspension. To control for uniform size distributions, the white suspension was immersed in a heated oil bath at 80°C with stirring for 10 minutes. The suspension was then centrifuged; removal of excess solvent and subsequently washed with deionized water. This step was done 3 times, before a vacuum drying procedure of 70°C at 12 hours. The dried powder was then calcined for 3-12 hours at 250°C to form the $In_2O_{3-x}OH_y$ phase nanorod structures.

Silver electrodes of greater than 500nm thicknesses were sputtered on the $In_2O_{3-x}OH_y$ nanorod films on quartz fiber substrate in a 4 pad square configuration spaced 0.5 cm apart. The four point probe current measurements were taken with a Keithley 2440 instrument, along with a Labview program that was created to carry out a voltage sweep from -5 to 5 V bias at time intervals of 1 minute. The photoillumination spot was approximately 1cm by 0.4cm between the silver electrodes which was achieved with the aid of a collimator and focusing lens while the monochromatic beam was controlled by a monochromator with linewidth of 2nm; the primary illumination was a white Xe/Hg lamp (Oriel Newport).

For EQE measurements, the photocurrent spectra were taken from a higher wavelength to a lower wavelength in order to reduce the effects of persistent photoconductivity. A chopper and lock-in amplifier were coupled to the monochromator. In addition, the wavelength intervals were taken 10 nm apart with a 20 minute interval between each current measurement taken at 5V bias. The measured current was then normalized against the dark current taken before photoillumination, and subsequently normalized with the incident photocurrent collected by a photodetector at each measured wavelength with the aid of a 50/50 beam-splitter in order to determine the quantum efficiency at each wavelength. All measurements were taken under various atmospheres, with the cryostat chamber pumped down to ~10^{-3} mbar before introducing H_2 or CO_2 or H_2+CO_2 (~1:1 pressure) at approximately 2.1 atm pressure.

For the photocurrent measurements, the monochromator was not initialized and hence the spot was a white beam while the photoillumination was turned on and off with an Arduino controller that regulated the shutter on the cryostat window. The copper holder is temperature controlled by a Lakeshore 331 controller, and a type K thermocouple feedthrough permits temperature monitoring of the sample with the thermocouple tip in contact with the edge of the sample film. Typically, the sample is heated to a temperature of 350K before carefully introducing liquid N_2 to lower the temperature, upon reaching approximately 200K the flow of liquid N_2 is stopped, and with the heater running at 50W the temperature is increased gradually back to 350K and thus creating a temperature loop. For optical spectroscopy measurements, a Perkin Elmer Lambda 1050 instrument with an integrating sphere accessory was used, where the integrating sphere exit port scintillon accessory was removed and replaced with the cryostat viewport. The sample film and the holder were adjusted to move the film as close as possible to the viewport. The cryostat instrument was covered with a black shroud in order to prevent parasitic light introduction into the integrating sphere. The window without the sample was auto-zeroed initially before proceeding with the measurements. Liquid nitrogen was introduced until reaching a temperature of 180K,

and then optical absorption measurements were taken at a temperature interval of 30K while the sample returned to room temperature naturally.

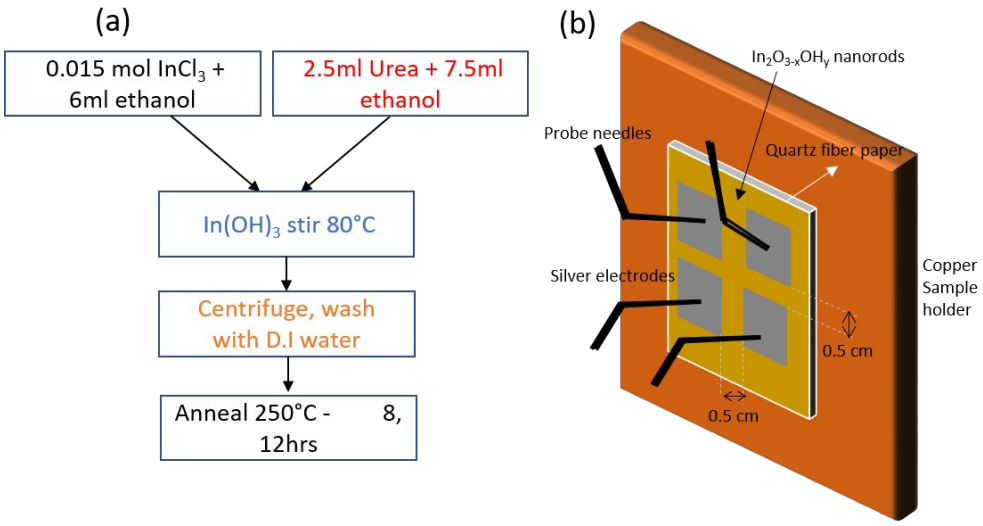

Supplementary Figure 1. (a) Flow chart schematic of sample preparation. (b) Sample holder schematic with $In_2O_{3-x}OH_y$ nanorod film with sputtered 500nm silver electrode pads. Tungsten probe needles are mechanically pinned onto the electrodes.

Potential surface Barrier determination

The following constants were used to determine the probability density function of the potential energy barrier associated with the surface of the $In_2O_{3-x}OH_y$ nanorod grains: $\gamma = 6 \times 10^{-13}$ cm^{-2}, $r_s = 0.3$, $\nu_s = 100 \times 10^{-13}$ cm^2/V by multiplying 20mV with 15 cm^2/Vs, $n_d = \sim 1 \times 10^{15}$ cm^{-3}. Mobility and concentration values were determined with a Hall Nanometrics HL5500 system on a 4 silver electrode pad arranged in square configuration on the corners of the sample on quartz fiber substrate. The confidence intervals were determined by ranging Beta with ±0.02 and stretched time constant with ±10 minutes.

EQE Spectra

Because the defect spectrum itself is of interest, the main absorption gaussian peak is not considered in the averaging of the trap energies.

	T1 (eV)	T2 (eV)	T3 (eV)	T4 (eV)	T5 (eV)	T6 (eV)	T7 (eV)	T8 (eV)	T9 (eV)	Average energy (eV) / density of states
S1 (Vac.)	2.4	2.52	2.55	2.65	2.75	2.84				2.64
S1 (H_2)	2.26	2.38	2.50	2.61	2.72	2.80	2.97			2.75

S1 (CO_2)	2.34	2.41	2.47	2.54	2.63	2.75	2.84	2.90		2.62
S1 (CO_2 + H_2)	2.33	2.57	2.65	2.74	2.84					2.69
S2 (Vac.)	2.36	2.40	2.47	2.55	2.61	2.70	2.82			2.51
S2 (H_2)	2.33	2.43	2.56	2.64	2.72	2.81	2.94			2.77
S2 (CO_2)	2.34	2.41	2.47	2.54	2.63	2.70	2.80	2.90		2.67
S2 (CO_2 + H_2)	2.28	2.39	2.47	2.55	2.65	2.74	2.84			2.58

Supplementary Table 1. The gaussian deconvolution of the EQE spectra with the sub-peak energy values, and the weighted average of the energies by the summation of the product of each subpeak with the peak area ratio of the defect spectra (tail of the EQE spectra) divided by the number of sub-peaks within the defect spectra.

Photoconductivity-temperature

Photoconductivity-temperature measurements under air, vacuum, H_2, CO_2 and H_2+CO_2 atmospheres are shown in **SI Figure 2**. The transition from ambient atmosphere to vacuum causes a large increase in photoconductivity, where it is likely that ambient moisture removal from the oxide surface remove physiosorbed hydroxyl groups. Noticeably the increase is greater for S2 air to vacuum transition with an associated low temperature ionization energy decrease, which indicate that the highly aged nanorods are less favorable to moisture retention. It is immediately obvious that the introduction of H_2 increases the photoconductivity value of both S1 and S2, while the introduction of CO_2 only slightly increases the photoconductivity, and H_2+CO_2 shows a similar photoconductivity increase from vacuum as that of CO_2 only atmosphere. For the H_2 only atmosphere, there is a significant hysteresis loop associated with the S2 photoconductivity, which indicate that H_2 reacts with pre-existing OH groups to desorb as H_2O, thus removing the active sites that enable dissociated and stable H^+ atoms. Hence, the stability of H adatoms can be shown in S2 where no hysteresis loop is observed at high temperatures, and the resistivity is low even at lower temperatures. This hints that H_2 dissociation is highly favorable at low temperatures which can compensate for the freezing out of thermally excited carriers. For H_2+CO_2, there is a lower ionization energy at high temperatures for S1, which indicates that charge carrier excitation is more favorable due to decreased densities of recombination centres or increased density of unoccupied states. Since the EQE results suggest that the latter is more likely, we attribute the lower ionization energy to increased defect densities that allow thermal hopping. A significantly different set of photoconductivity temperature curves are seen with S0 with aging of 2 hours at 250°C. where a

distinctive hump is seen at ~170-250K, which corresponds to carrier hopping mechanisms in amorphous material systems.

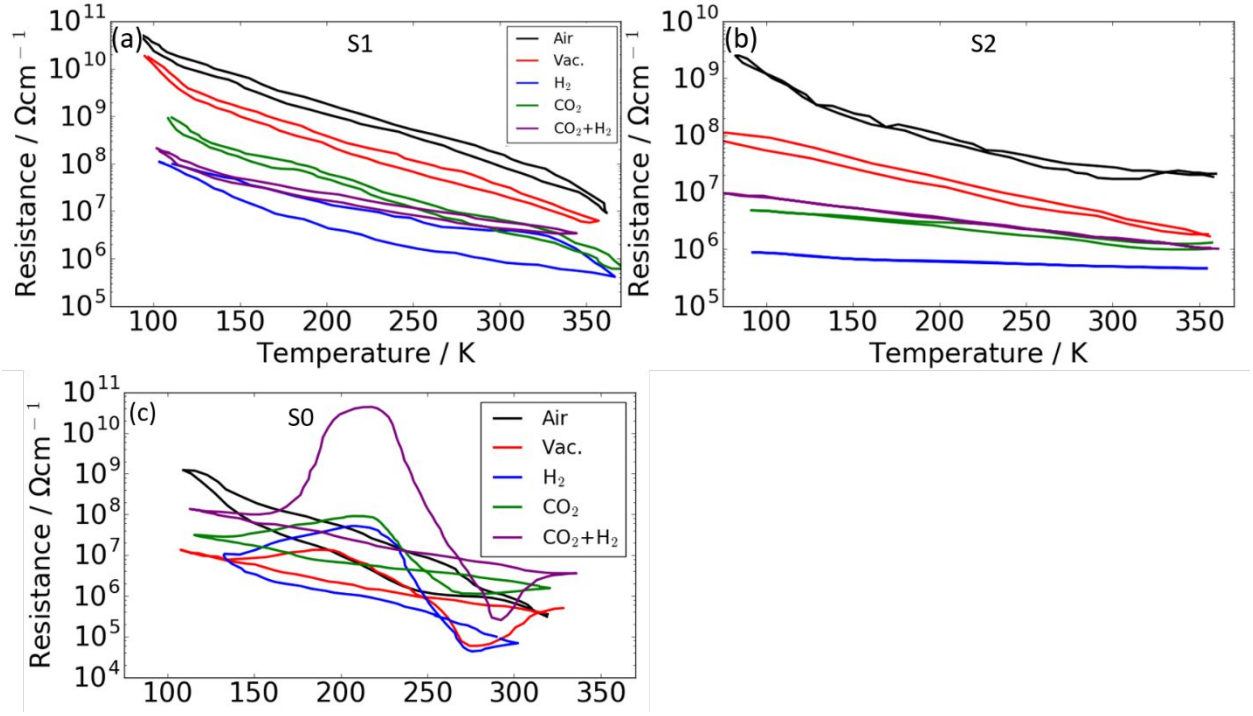

Supplementary Figure 2. Photoconductivity - temperature trends of S1 and S2 and S0 in (a) and (b) and (c), respectively. For S1 and S2, the photocurrent increases from air to vacuum, and significantly from vacuum to H_2, but the decrease is smaller for CO_2 and the photocurrent values are similar between CO_2 and H_2+CO_2.

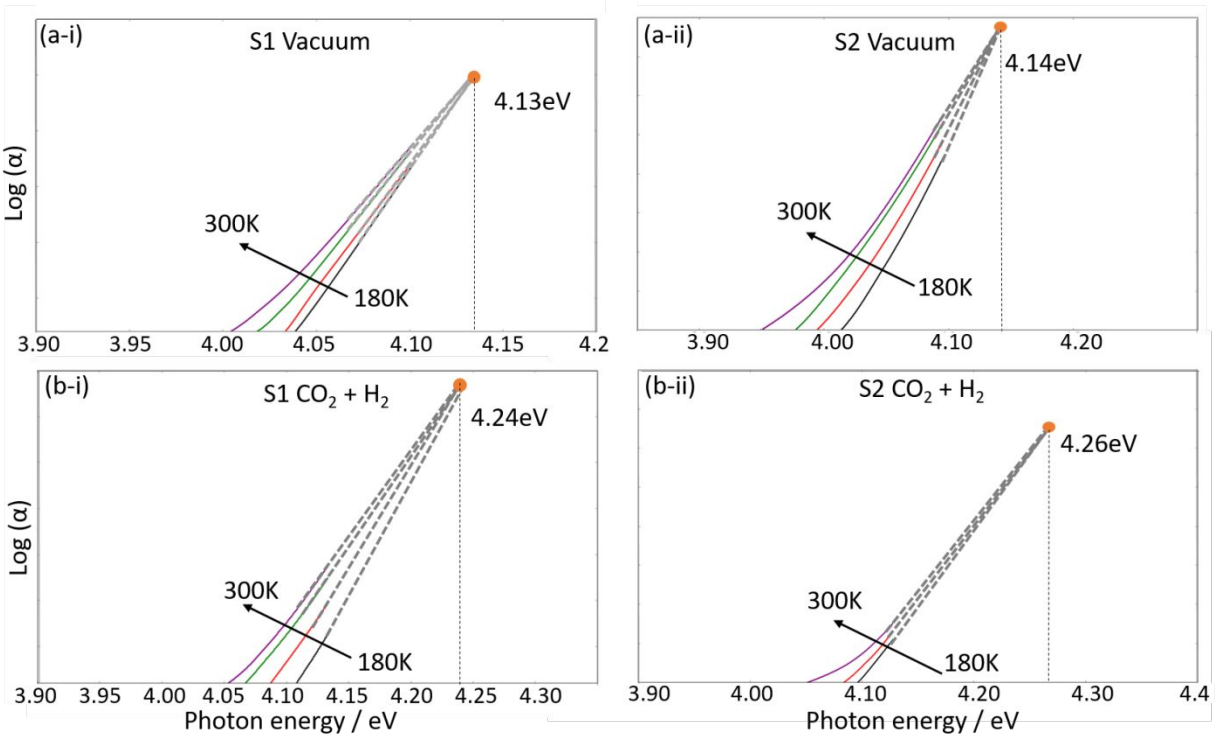

Supplementary Figure 3. Optical absorption spectroscopy plots of S1 (i) and S2 (ii) in Vacuum (a), and CO_2+H_2 (b). The absorption plots were taken from 180K to 300K sample temperatures. The extrapolated grey dotted lines end at the Urbach focus of 4.14 and 4.18eV for S1 and S2, respectively, in vacuum, and 4.23 and 4.27eV, respectively, in CO_2+H_2.

EPR measurements

For the EPR measurements, a Bruker X-band CW EMX EPR spectrometer equipped with a 10'' electromagnet and an ER 4119HS resonator was applied for signal detection. The parameters set for the EPR measurements in this study were: a microwave frequency of 9.34 GHz, a microwave power of 20 db, a modulation amplitude of 4.0 G, a sweep width of 3276.0 G, a sweep time of 200 s, a receiver gain of 20 db, a scan number of 3, a modulation frequency of 100 kHz, a modulation phase of 180 degrees, a time constant of 0.01 ms, and a points per modulation amplitude of 10. The spectra were recorded at ~300 K. After illuminating the S2 sample with the blue laser the laser was turned off and after waiting for 10 minutes a subsequent scan showed that the secondary peak was not present. A 535nm wavelength green laser was subsequently illuminated on the sample for 3 minutes. The scan under green light showed no secondary peak but a small decrease in signal intensity, showing that some paramagnetic centres were lost during photo-excitation by sub band gap wavelengths (**SI Figure 4**).

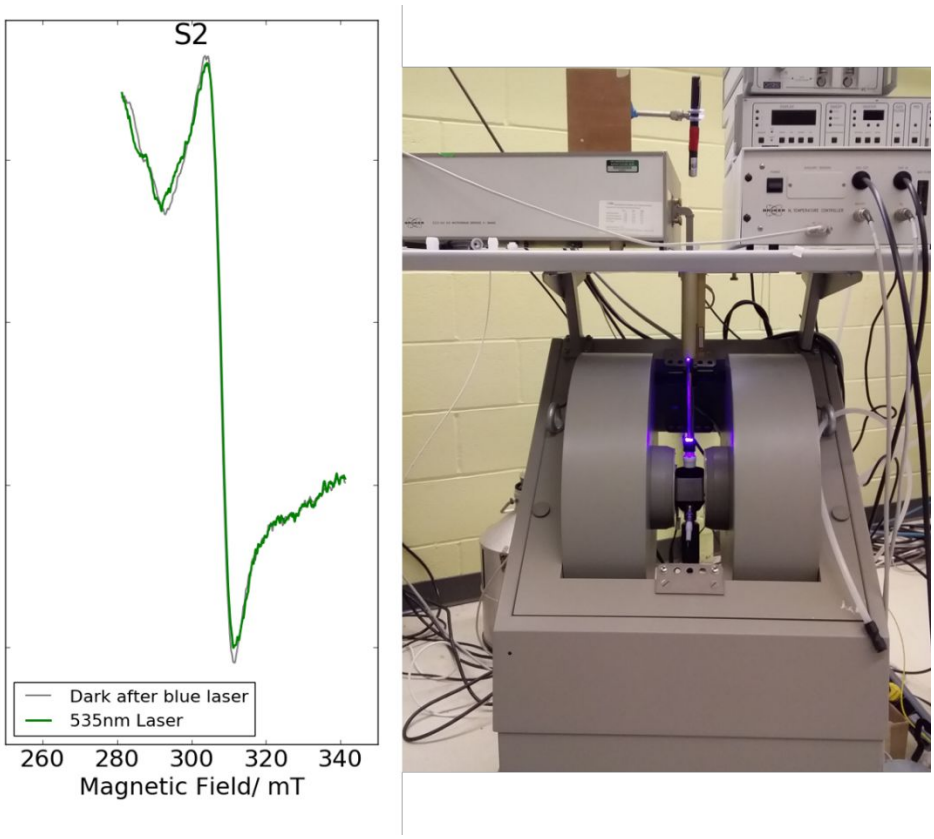

Supplementary Figure 4. The EPR spectra taken after turning off the blue laser for 10 minutes, shown in grey; and the spectra taken under green 535 laser photoillumination for 3 minutes. The next image shows the EPR measurement being taken under a blue laser. Unfortunately, the laser alignment was highly sub-optimal due to time and spatial constraints.